# Signatures of Fano Interferences in the Electron Energy Loss Spectroscopy and Cathodoluminescence of Symmetry-Broken Nanorod Dimers

**Nicholas W. Bigelow,[†] Alex Vaschillo,[†] Jon P. Camden,[‡] and David J. Masiello[†,*]**

[†]Department of Chemistry, University of Washington, Seattle, Washington 98195-1700, United States and [‡]Department of Chemistry, University of Tennessee, Knoxville, Tennessee 37996-1600, United States

**ABSTRACT** Through numerical simulation, we predict the existence of the Fano interference effect in the electron energy loss spectroscopy (EELS) and cathodoluminescence (CL) of symmetry-broken nanorod dimers that are heterogeneous in material composition and asymmetric in length. The differing selection rules of the electron probe in comparison to the photon of a plane wave allow for the simultaneous excitation of both optically bright and dark plasmons of each monomer unit, suggesting that Fano resonances will not arise in EELS and CL. Yet, interferences are manifested in the dimer's scattered near- and far-fields and are evident in EELS and CL due to the rapid $\pi$-phase offset in the polarizations between super-radiant and subradiant hybridized plasmon modes of the dimer as a function of the energy loss suffered by the impinging electron. Depending upon the location of the electron beam, we demonstrate the conditions under which Fano interferences will be present in both optical and electron spectroscopies (EELS and CL) as well as a new class of Fano interferences that are uniquely electron-driven and are absent in the optical response. Among other things, the knowledge gained from this work bears impact upon the design of some of the world's most sensitive sensors, which are currently based upon Fano resonances.

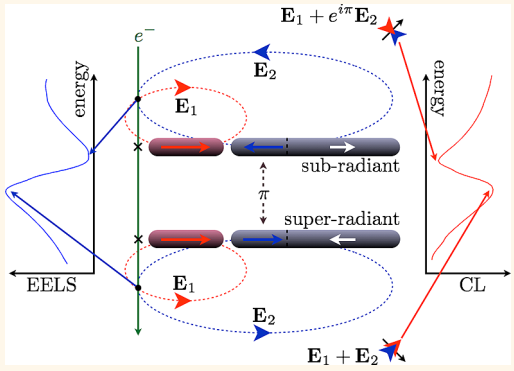


**KEYWORDS:** Fano resonances · plasmonics · electron energy loss spectroscopy · cathodoluminescence

Interference is ubiquitous in nature. It can be heard in the discord of out-of-tune musical instruments, seen in the skipping of a rock on a still pond, and evidenced as electrons are subjected to the famous double slit. In 1961, Ugo Fano explained the asymmetric line shapes observed in the spectrum of helium vapor under electron impact as being due to the interference between the scattering amplitudes for the incident electron to scatter directly and to scatter *via* autoionization.[1] A similar asymmetric line shape is observed in the optical scattering spectra of metal nanostructures when a bright plasmon mode is resonantly coupled to a dark plasmon.[2−6] From the excited bright mode, energy is transferred nonradiatively to the dark mode and back to the bright, with a $\pi$-phase offset. Both excitations superimpose and destructively interfere on the bright mode, which radiates a signal into the far-field that is characterized by an asymmetric Fano line shape.

Electron spectroscopies like electron energy loss spectroscopy (EELS) and cathodoluminescence (CL) are rapidly emerging as important tools in the characterization of plasmon resonances due to their sub-angstrom spatial resolution.[7−9] EELS has been used to investigate the plasmonic properties of a wide variety of nanostructures, including cubes,[10] spheres,[11,12] prisms,[13,14] split-ring resonators,[15] rods,[16−19] and complex star-like structures.[16] Nanoparticle aggregates have also been explored with EELS, including nanodisk multimers,[2] dolmen-like structures,[4] sphere trimers,[6] asymmetric sphere dimers that are homogeneous in composition,[12] cube dimers,[20] planar triangular dimers and trimers,[21] and nanorod dimers.[19,22,23] Over the past few years, a number of experimental and theoretical

* Address correspondence to masiello@chem.washington.edu.

Received for review March 7, 2013 and accepted April 17, 2013.

**Published online April 17, 2013**
**10.1021/nn401161n**

efforts have exploited EELS and CL to better understand how nanoparticles interact, broadcast energy to the far-field, and store energy in the near-field.[8,24−26] The signatures of electromagnetic hot spots and the relationship between the local density of states and EEL probability are now well-understood.[19,20,27,28] Yet, in light of this wealth of knowledge, it is still unclear if and under what conditions Fano interferences will appear in EELS and CL, and what the optical response will be in these situations. Since plasmon modes that are optically dark may be bright under electron excitation, it seems that Fano interferences will be absent in electron spectroscopies. To date, all nanostructures that display Fano resonances in their optical spectra reported in the literature have not shown them in EEL or CL spectroscopies at the same energies.[2,4] Advances in the energetic sensitivity of EELS will play an important factor in finding electron-induced Fano-like interference features, as they can be spectrally sharp and difficult to observe in the laboratory.[29−31] It is the purpose of this article to guide experiment in this pursuit by predicting the electron-induced optical frequency responses of metal nanorod dimers *via* numerical simulation.

Both EEL and CL spectroscopies are initiated by a collimated stream of swift electrons, often originating from a scanning transmission electron microscope (STEM), impinging upon a target. Most electrons are elastically scattered. However, inelastic scattering events occasionally occur as electrons suffer kinetic energy losses in exchange for the creation of elementary and/or collective excitations in the target.[8] For noble metal nanostructures, it is the latter type of response that is important, corresponding to surface plasmon resonances that are usually excited at optical frequencies.

Due to the differing selection rules between the electron probe, which acts as a nanolocalized source of broad-band electromagnetic radiation, and a far-field source of monochromatic light like a plane wave, both optically bright and dark plasmon modes of the target may be excited by the electron. Only those modes with a net dipole moment are capable of outcoupling their energy to the far-field and are identifiable in CL spectra. Yet both bright and dark modes may contribute to the EEL spectrum. The EEL signal

$$\Gamma_{\mathrm{EELS}}(\hbar\omega) = \frac{e}{\pi\hbar^2\omega}\int \mathrm{d}t\,\mathrm{Re}\{e^{-i\omega t}\mathbf{v}\cdot\mathbf{E}_{\mathrm{ind}}(\mathbf{r}(t),\omega)\} \quad (1)$$

is determined from the work done on the impinging electron, located at $\mathbf{r}(t)$, by its induced electric field, $\mathbf{E}_{\mathrm{ind}}$. $\Gamma_{\mathrm{EELS}}$ represents the probability for the electron to lose kinetic energy to the target per unit of energy loss suffered by the passing electron. When the STEM is scanned in the vicinity of the target, it is mainly the near-field components of $\mathbf{E}_{\mathrm{ind}}$ that contribute to $\Gamma_{\mathrm{EELS}}$. While the total CL signal

$$\Gamma_{\mathrm{CL}}(\hbar\omega) = \frac{cr_S^2}{4\pi^2\hbar^2\omega}\int \mathrm{d}\Omega|\mathbf{E}_{\mathrm{ind}}(\mathbf{x}_S,\omega)|^2 \quad (2)$$

is determined from integrating the radiative energy flux carried by the far-field components of the induced electric field, $\mathbf{E}_{\mathrm{ind}}(\mathbf{x},\omega) \sim \mathbf{f}(\Omega)e^{ikr}/r$, over the surface of a distant flux screen of radius $r_S = |\mathbf{x}_S|$, with $kr_S \gg 1$.[8] It represents the number of photons emitted in all directions at the energy $\hbar\omega$ per incoming electron. Both of these expressions are parametrized by the path of the electron, described by $\mathbf{r}(t)$. In this way, EELS is characterized by a near-field probe and near-field observation, while CL is characterized by a near-field probe and far-field observation. This is in contrast to optical spectroscopy, where both the excitation source and observation are in the far-field. It is also important to note that aggregates of nanoparticles may support hybridized plasmon modes that are super- or subradiant in character. Neither mode is dark, and both may store electromagnetic energy in the near-field as well as carry electromagnetic energy to the far-field. These particular properties will be important in the following in understanding interference effects in optical and electron spectroscopies.

In this paper, we explore the consequences of Fano interferences in electron and optical spectroscopies between multipolar plasmonic excitations in symmetry-broken nanorods that are heterogeneous in material composition and asymmetric in length. These interferences arise from the phase offsets between the electric dipolar (bright) plasmon of a Pd rod with the electric quadrupolar (dark) plasmon of a nearby Ag rod. Both of these plasmonic responses are excited by the electron beam and may hybridize into super- and subradiant plasmons that store and radiate electromagnetic energy in the near- and far-field. The relative size of each monomer unit is tuned so that these Pd and Ag plasmon resonances overlap spectrally, and depending upon the position of the electron beam, their interference can be read out in the near-field *via* EELS and in the far-field *via* CL. In addition, we identify the conditions where both the far-field optical and CL scattering evidence Fano interferences as well those conditions where interferences are absent in the optical response but are present in the CL. The understanding gained from this particular system guides us in predicting if and how interference features will arise in the electron and optical spectroscopies of more general systems. This will be of significant importance particularly in the development of high-sensitivity plasmon-based sensors, where Fano resonances currently underlie some of the world's best.[32−34]

## RESULTS AND DISCUSSION

**Fano Interferences in Electron Energy Loss Spectroscopy.** To examine the signatures of Fano interferences in EELS and CL, we perform numerical simulations on a

nanorod dimer using our recently implemented electron-driven discrete-dipole approximation (*e*-DDA).[19] The *e*-DDA is a generalization of the DDA concept[35,36] to include the electron source of a STEM instead of a plane wave. In this article, the *e*-DDA is further extended to compute CL. For simplicity in presentation, a description of the theory and numerical implementation of the *e*-DDA is deferred to the Methods section.

*Symmetry Breaking*. We begin by engineering a metal nanostructure that supports Fano resonances in both optical and electron spectroscopies. High aspect ratio rods make an ideal test bed for these studies because they support a multipolar progression of alternating, longitudinally polarized bright and dark plasmon modes that can be spectrally tuned by altering the rod's composition and length. Asymmetric nanorod dimers offer the possibility for an optically dark plasmon on one monomer unit to spectrally overlap an optically bright mode on the other. In addition, the symmetry of such a heterodimer is lowered in comparison to the corresponding monomer in such a way that the two modes may couple. More precisely, before adding a second particle, the odd-parity (bright) and even-parity (dark) modes of the rod monomer do not interact because they belong to different irreducible representations of the $C_{\infty v}$ point group (neglecting the presence of the electron probe). However, after breaking the symmetry by the addition of a second particle, both even- and odd-parity plasmons transform according to the same irreducible representation of the $C_s$ group and, therefore, can interact. Further, the spatial symmetry-breaking induced by the placement of the electron beam itself is enough to allow odd- and even-parity plasmons on a single rod monomer to interact, but tuning the spectral positions of these modes so that they overlap is challenging.

Figure 1 presents the optical and electron spectra of a symmetry-broken Pd–Ag nanorod dimer as well as the spectra of their corresponding monomers. We choose these metals because the Pd dipole is quite lossy in the optical regime and makes an ideal candidate for the requisite *broad* and *bright* mode, while the Ag quadrupole is *narrow* and *dark*. Other choices of metals that have similar properties may also serve as ideal candidates. As depicted in the top panel, the left rod is composed of Pd and has a length of a 50 nm, while the right rod is composed of Ag and has a length of 100 nm; they both have a 10 nm radius, are colinearly arranged, and are separated by a gap of 1 nm. The lengths of each monomer unit have been adjusted so that the spectrally narrow and optically dark electric quadrupole ($n$ = 2) and optically bright electric hexapole ($n$ = 3) plasmon of the Ag rod (blue curve) overlap the broad-band optically bright electric dipole ($n$ = 1) plasmon of the Pd rod (red curve) as displayed in the middle panel.

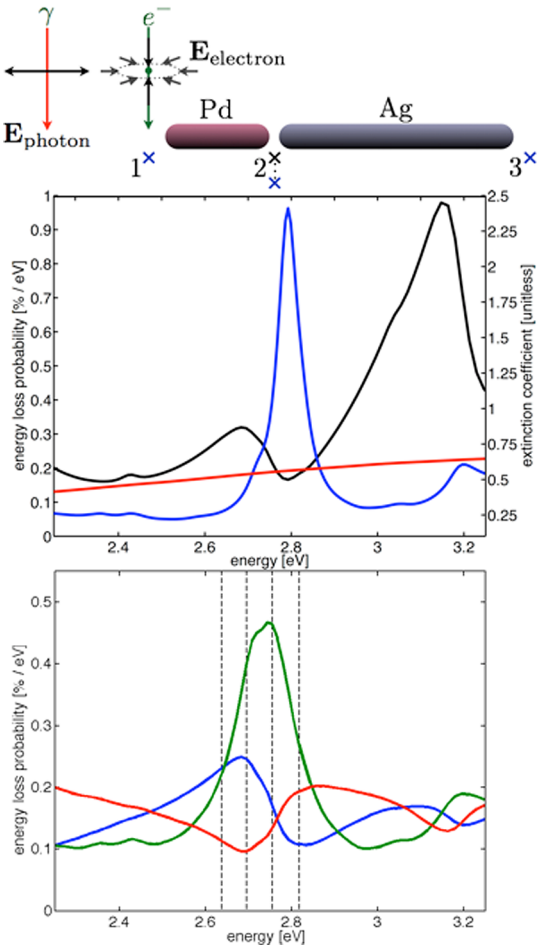


**Figure 1. Optical and electronic responses of a symmetry-broken Pd–Ag nanodimer. Top panel: Depiction of the dimer system is displayed together with the locations of three positions of the electron beam used to interrogate the system; positions 1 and 3 are computed 1 nm off of the respective rod's tip and have an impact parameter $b_y$ = 1 nm off of the rod's surface (11 nm from the rod's center); position 2 is centered in the junction and has an impact parameter that ranges between 1 and 30 nm off of the rod's surface ($b_y$ = 11–40 nm from the junction center) in addition to the junction center ($b_y$ = 0 nm). Middle panel: Optical spectrum of the mixed-metal dimer is presented (black) as are the EEL spectra of the Ag (blue) and Pd (red) monomers excited at their ends. A pronounced Fano interference "dip" is apparent near 2.80 eV in the optical spectrum. Bottom panel: EEL spectra corresponding to each of the three positions in the top panel are presented. Position 1 is displayed in blue; position 2 (computed at $b_y$ = 30 nm) is displayed in red, and position 3 is displayed in green; the EEL probability at position 2 is multiplied by 5 to aid in visualization. Fano interference features are clearly visible in the EEL spectra taken from positions 1 and 2. No interference is observed in the EEL spectrum at position 3.**

On the basis of these symmetry properties, we expect to find a Fano interference feature in the optical spectrum of the dimer in the vicinity of the Pd dipole–Ag quadrupole overlap, due to the near-field energy exchange between bright and dark modes and the subsequent interference originating from their relative phase offset. Indeed this is true, as exemplified by the black curve in the middle panel. A pronounced Fano

"dip" in the extinction spectrum is visible near 2.80 eV, where the Ag quadrupole (blue curve) and Pd dipole (red curve) plasmons interfere. Interestingly, no such pronounced feature occurs if both rods are of the same material composition, due to the poor spectral overlap between super- and subradiant plasmons. This may not be true, in general, but is true if both rods are Pd or both are Ag.

*Electron-Driven Fano Resonances.* The question now remains of what the EEL response will be when the STEM is rastered across different points surrounding the target. The bottom panel of Figure 1 presents the EEL spectra corresponding to the three different spatial points indicated in the top panel. In all calculations, an aloof 0.10 MeV electron beam is used to perturb the system. Interestingly, we see that three qualitatively different responses are predicted.

The blue curve is the EEL spectrum resulting from an electron beam placed at position 1. Comparison with the optical spectrum in the middle panel (black curve) shows that both exhibit a similar Fano line shape and associated dip near 2.80 eV. However, the mechanism for this interference in EELS is somewhat different from that occurring in optical spectroscopy. First, both the bright Pd dipole plasmon and dark Ag quadrupole plasmon are simultaneously coexcited to some extent by the electron beam. For loss energies between ~2.45 and 2.65 eV, the passing electron is able to efficiently pump energy through the Pd dipole into the super-radiant hybridized plasmon mode of the dimer (displayed in the caption figure). While for loss energies exceeding ~2.70 eV, the subradiant hybridized plasmon mode (displayed in the caption figure) is more energetically favorable yet is difficult to excite with the electron beam positioned at point 1. This is because the polarization of the electron's evanescent electric field (see eq 4 below) pins the orientation of the Pd dipole and forces the polarization of the Ag quadrupole to flip its phase by $\pi$ at loss energies greater than ~2.70 eV. For these reasons, there is a higher EEL probability below the Fano resonance frequency (~2.75 eV) than above. It is worth noting that an Alzar model[37] describing the nanorod dimer as a system of coupled springs both driven out of phase also reproduces these Fano interferences.

A strikingly different EEL spectrum results when the electron beam is positioned at point 2 (red curve). There, the subradiant hybridized plasmon mode is more efficiently pumped, which leads to an inverted Fano line shape that is optically inaccessible. At loss energies above ~2.70 eV, the subradiant mode is resonant and, indeed, the EEL probability is larger there. For loss energies below ~2.70 eV, the super-radiant mode is more energetically favorable but is difficult to excite with the electron beam near the junction. This is because the polarization of the electron's evanescent electric field pins the antibonding arrangement of polarizations in the vicinity of the junction, and either the Pd dipole or Ag quadrupole must flip the phase of its polarization by $\pi$ to accommodate the super-radiant configuration. The probability for the passing electron to lose energy into this arrangement is, consequently, smaller.

When the electron beam is rastered to position 3 (green curve), no interference is observed in EELS. This is because the electron beam is perfectly positioned to drive the Ag quadrupole with high probability. At loss energies below ~2.75 eV, the quadrupole funnels energy into the super-radiant plasmon mode, while for loss energies greater than ~2.75 eV, the quadrupole funnels energy into the subradiant plasmon mode. At this position, the electron beam only pins the polarization of the Ag quadrupole, leaving the distant Pd dipole flexible to flip its phase by $\pi$ between super- and subradiant orientations. However, the electric near-field induced by this $\pi$-phase offset of the Pd rod provides only a small perturbation to the near-field of the Ag quadrupole acting back upon the electron at position 3. Therefore, almost no interference signature is manifested in the EEL spectrum at this position of the electron beam.

At positions 1 and 2, there is a corresponding interference in the electric near-field generated by the superposition of oscillating bright and dark plasmonic modes. Figure 2 displays the spectrum of the unit normalized induced electric-field magnitude (green curves) evaluated at positions 1 and 2 of the electron beam, together with the corresponding EEL spectrum (red curves) at each position. Pronounced destructive and constructive interference dips and peaks in the field magnitude are clearly visible at the loss energies where the electron-induced Fano resonances occur. These spectral features impact the EEL probability as governed by the loss function in eq 1, opening up effective transparency and opacity windows of minimized and maximized EEL probability.

In the top left panel of Figure 2 corresponding to position 1, the electric field minimum near 2.75 eV is due to the polarization flip of the Ag rod's quadrupole plasmon. Because the superposition of induced electric fields at position 1 is constructive before the polarization flip, it becomes destructive afterward. This is the scenario portrayed in the caption figure. In the top right panel corresponding to position 2 with an impact parameter $b_y$ = 11 nm, the electron beam pins the locally antibonding arrangement of polarizations, with a correspondingly destructive interfering induced electric field in the junction. This is the energetically favorable plasmon configuration at loss energies greater than ~2.80 eV. At lower loss energies, where the super-radiant mode is resonant, either the Pd dipole or Ag quadrupole must flip its phase to accommodate the new configuration and the superposition of induced electric fields becomes constructive in character.

To further elucidate the underlying plasmonic motion responsible for these interference effects, we

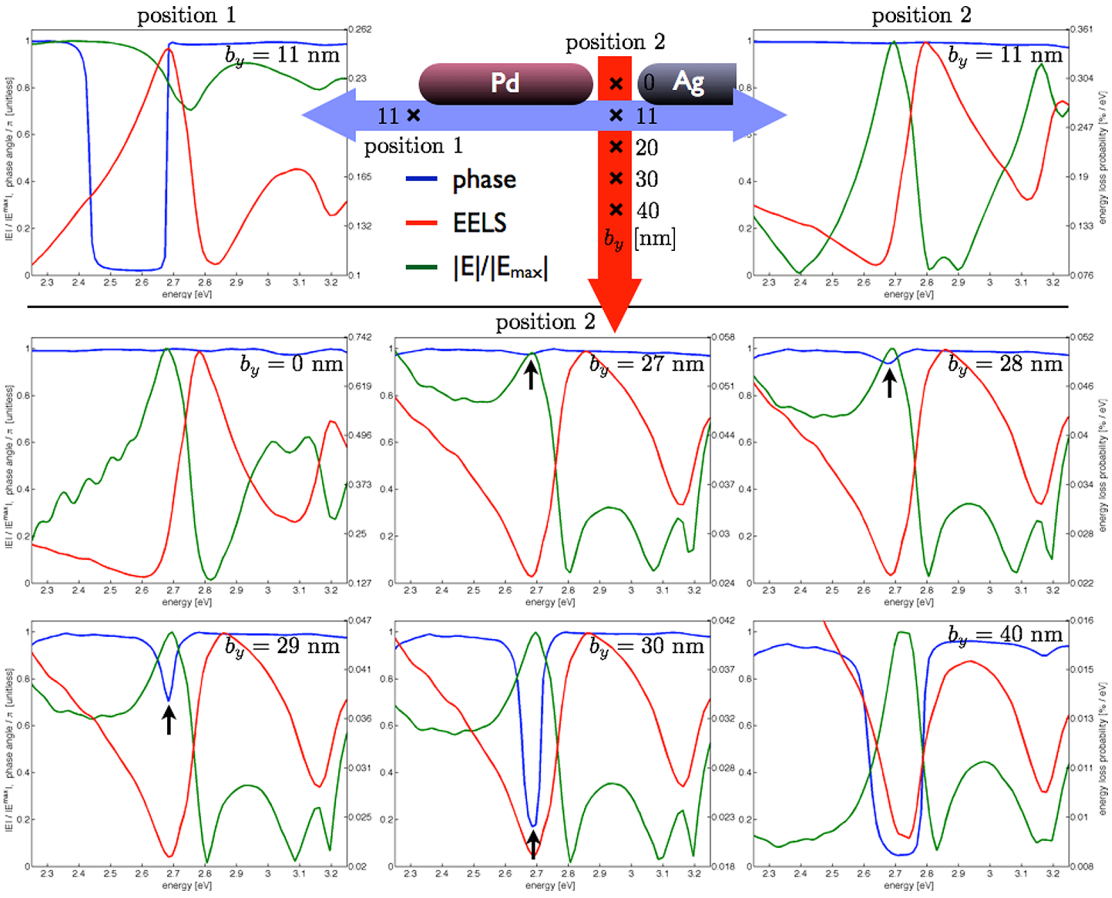


**Figure 2. EEL spectrum (red) and magnitude (green) and phase (blue) of the scattered electric near-field evaluated at positions 1 and 2 where electron-induced Fano interferences occur. The electric field magnitude is normalized so that its maximum takes a value of 1 in each panel. Top left panel: At position 1, the electron beam is oriented to pump the super-radiant plasmon mode of the dimer through the Pd dipole between ~2.45 and 2.65 eV. However, as the loss energy approaches 2.75 eV, the subradiant plasmon becomes resonant and the phase of the polarization of the Ag quadrupole flips from 0 to $\pi$, resulting in a destructive interference of the induced electric field at position 1 and a corresponding Fano resonance near 2.75 eV. Top right panel: At position 2, when the electron beam is placed at $b_y$ = 11 nm, there is no Fano resonance. This is due to the fact that the electron beam is locally pinning the subradiant plasmon, which maintains a relative phase offset of $\pi$ for all loss energies. Bottom panels: Nonetheless, a Fano resonance can be activated at position 2 by rastering the electron beam to larger impact parameters, $b_y$, away from the junction within the impact plane. As $b_y$ increases from 0 to 40 nm, a pronounced relative phase offset rapidly grows between monomer units (black arrows). At these positions, the electron beam is oriented to pump a locally antibonding arrangement of the plasmon polarization in the vicinity of the junction, which is consistent with the subradiant plasmon configuration. The corresponding electric field induced by this local configuration is destructive. However, as the loss energy is lowered to ~2.70 eV, the super-radiant plasmon mode becomes resonant and the Pd dipole flips its phase by $\pi$ to accommodate the resonant configuration. This forces the relative plasmon phase delocalized across the dimer to fall to 0 near ~2.70 eV and leads to a constructive interference of the associated induced electric field and an associated Fano resonance. Position 3 is not investigated since no significant interference in the EEL spectrum is observed at impact parameters, $b_y$, near that point.**

additionally plot in Figure 2 the relative phase $\phi$ (blue curves) of the electron-induced electric field evaluated at the position of the impinging electron. Equation 1 dictates that the EEL signal is determined from the work done by the electron's induced electric field acting back upon the electron. However, in the case of the nanorod dimer, the electron "sees" the super-position of electric fields scattered from both the Pd and Ag rods as $\mathbf{E} = \mathbf{E}_{Pd} + e^{i\phi}\mathbf{E}_{Ag}$, with magnitude

$$|\mathbf{E}(\mathbf{x}_j)| = (|\mathbf{E}_{Pd}(\mathbf{x}_j)|^2 + |\mathbf{E}_{Ag}(\mathbf{x}_j)|^2 + 2|\mathbf{E}_{Pd}(\mathbf{x}_j)||\mathbf{E}_{Ag}(\mathbf{x}_j)|\cos\phi)^{1/2} \quad (3)$$

with $j$ = position 1, 2. The dependence of $\phi$ upon the loss energy indicates how the polarization of each monomer unit contributes to the total polarization of the super- or subradiant plasmon delocalized across the dimer. When the two monomers are out of phase by $\pi$, they participate in the subradiant hybridization, while they compose the super-radiant hybridization when they are in phase.

At position 1 (top left panel), a pronounced phase shift (blue curve) occurs rapidly near 2.70 eV as the plasmonic motion transforms between super- and sub-radiant configurations. Corresponding to this $\pi$-phase shift of the Ag quadrupole is a Fano resonance in the EEL spectrum (red curve). Interestingly, even though there is an asymmetric EEL line shape at position 2 at an impact parameter of $b_y$ = 11 nm, there is no Fano

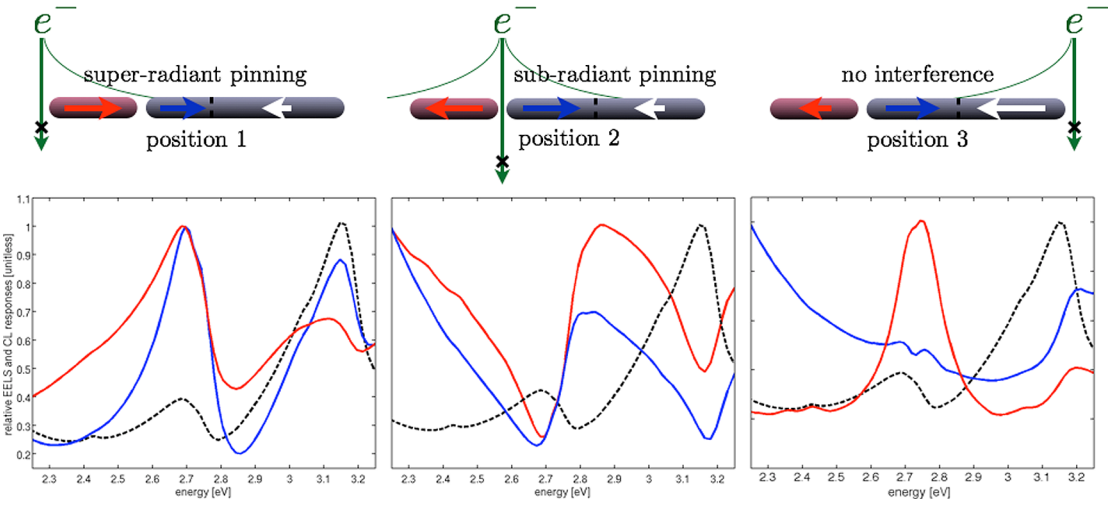


**Figure 3. CL (blue) and EEL (red) spectra taken from positions 1, 2, and 3 as well as the optical extinction spectrum (dashed black) of the Pd−Ag nanorod dimer. Each curve is normalized so that its maximum takes a value of 1 in each panel. Left panel: At position 1, all three spectroscopies display Fano interferences and encode qualitatively the same information in their spectra. Middle panel: Strikingly different spectra are observed at position 2 at $b_y$ = 30 nm, due to the location of the electron beam near the junction. At this position, an antibonding (optically dark) plasmon is responsible for establishing the Fano interference. This new Fano feature is manifested in both EELS and CL but has no optical analogue. Right panel: Due to the distant location of position 3, only the Ag particle is appreciably excited and any phase reorientation of the Pd dipole acts only as a perturbation to the induced electric field of the Ag plasmon. Therefore, no significant interference effect is present in either of the electron spectroscopies.**

resonance. This can determined by examining the plasmon's relative phase, which remains near $\pi$ for all loss energies. The rigidity of this phase is due to the fact that the swift electron passing near to the junction mainly feels the strong local polarization of the junction, which is pinned in an antibonding configuration. Plasmon polarization components that are distant from the junction have little effect upon the phase of the field in the junction. However, as the electron beam is rastered out of the junction to larger impact parameters, a variety of unusual Fano interference features can be initiated.

The lower six panels of Figure 2 display the birth and evolution of a Fano resonance in EELS at position 2 as a function of impact parameter $b_y$ = 0−40 nm. In particular, between $b_y$ = 27 and 30 nm, the plasmon's phase drops rapidly from $\pi$ down to 0 near 2.70 eV. This is due to the fact that, in addition to the locally pinned antibonding arrangement of the plasmon polarization in the vicinity of the junction, there is a more distant polarization component of the Pd monomer that flips its phase to accommodate the super-radiant configuration that is resonant at ∼2.70 eV. When the beam is close to the junction, the electric field scattered from this component is small in comparison to that generated by the locally antibonding plasmon configuration. However, at larger impact parameters, it becomes more important and is responsible for the rapid phase change as well as the corresponding constructive interference of the scattered electric field and resulting Fano interference. Such an electron-driven Fano resonance is inverted with respect to that occurring at position 1 and is absent in optical spectroscopy because it stems from an antibonding plasmon configuration that is optically inaccessible.

**Fano Resonances in Cathodoluminescence Spectroscopy.** We now turn to the question of what, if any, will be the signatures of Fano interferences in CL and will they be observable in situations where there is no corresponding optically driven Fano resonance. In order for there to be a CL response, eq 2 dictates that there must be an electron-induced radiative emission of energy carried to the far-field. This means that only plasmon modes that have a net dipole moment will be visible in CL spectra. However, in the case of the Pd−Ag nanorod dimer studied herein, both of the previously discussed electron-driven Fano interferences involve the excitation of super- and subradiant plasmon modes. Both of these hybridized excitations have a net dipole moment and can broadcast electromagnetic energy into the far-field. This means that, in principle, it should be possible for asymmetric Fano line shapes to be observed in CL.

Figure 3 displays the CL (blue curves) and EEL (red curves) spectra of the symmetry-broken Pd−Ag nanorod dimer displayed in Figure 1, corresponding to the positions 1−3 of the electron beam. Each panel also displays the optical scattering spectrum (black dashed curves) of the same dimer for comparison. Since all three spectra have different units, we have chosen for simplicity to rescale each curve so that its maximum value has a magnitude of 1.

In the left panel of Figure 3 corresponding to position 1, the first Fano resonance peak near 2.70 eV is common to all three spectroscopies. It arises from the

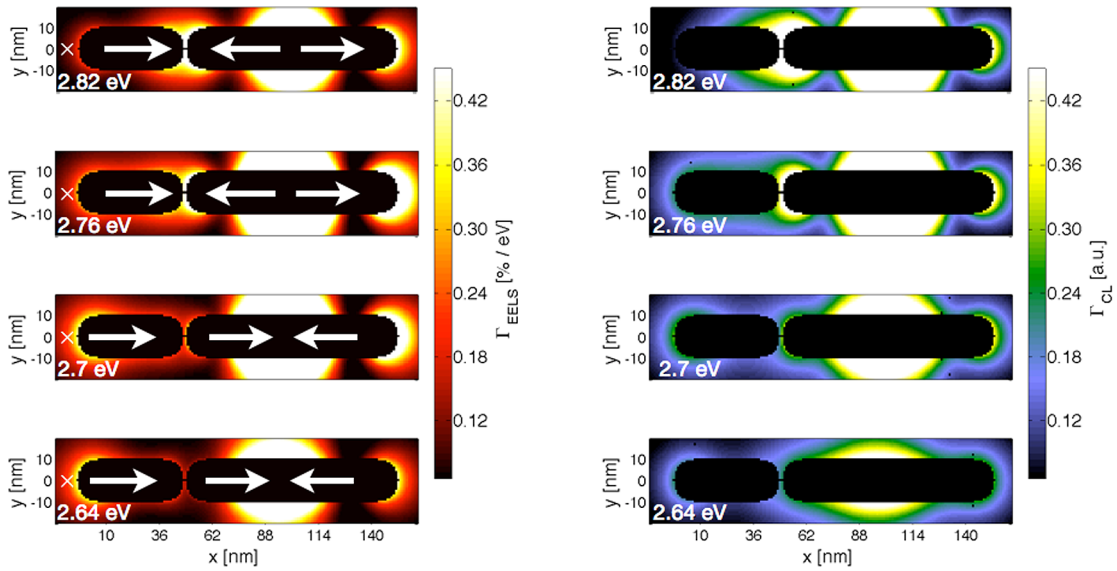


**Figure 4. EEL probability maps (left column) and CL maps (right column) of the Pd−Ag nanorod dimer computed at the four loss energies indicated by the vertical black dashed lines in Figure 1. Regions of high EEL probability correspond to nodes in the plasmon's polarization.[19] The latter is indicated by overlaid white arrows, with a relative phase dictated by the electron beam source located at the × position. The reorientation of the direction of the underlying monomer plasmons composing the hybridized dimer plasmon as it transitions from super-radiant to subradiant character is visible in both the EEL and CL maps.**

emission of radiation from the Pd dipole−Ag quadrupole super-radiant plasmon powered by the Pd dipole. All three spectra are qualitatively similar, and they encode basically the same information.

This is no longer true when the electron beam is moved to position 2 at the impact parameter $b_y$ = 30 nm, as seen in the middle panel of Figure 3. There, the electron spectroscopies are both capable of exciting the Pd dipole−Ag quadrupole subradiant mode with high probability *via* the Ag quadrupole plasmon. Neither of these hybridized plasmons of the dimer (induced by EEL or CL probes) are optically dark, and both may store electromagnetic energy in the near-field and liberate energy to the far-field in the form of radiation. This is why the EEL and CL responses look so similar. Further, this provides a surprising example of an electron-driven Fano interference that is observable in the far-field (through CL) but has no optical signature. To our knowledge, this is the first prediction of a new class of Fano resonance that is accessible by the differing selection rules of the electron beam, and that can be selectively excited based on the beam's position.

Lastly, in the right panel of Figure 3 corresponding to position 3, there is no significant interference effect in either of the electron spectroscopies. Just as in the case of EELS at position 3, the polarizations of the Ag quadrupole, and at lower loss energies, the Ag dipole plasmons are pinned by the electron beam, and the induced field generated by either orientation of the distant Pd dipole acts only as a perturbation in both the near- and far-fields. However, since the Ag dipole plasmon scatters a radiation field that is relatively much stronger than those scattered by the super- and subradiant (Pd dipole−Ag quadrupole) plasmon modes of the dimer, the latter two plasmon modes appear as small spectral features on the shoulder of the Ag dipole resonance in CL. This differs from the EEL response where the energetically distant Ag dipole does not play as significant of a role in the near-field.

Figure 3 displays the spectral correlation between EEL and CL responses across two Fano resonances of the Pd−Ag nanorod at three specific spatial electron beam positions. In Figure 4, we now present the corresponding spatial correlations between aloof EELS and aloof CL at four specific energies, 2.64, 2.70, 2.76, and 2.82 eV, indicated by the vertical black dashed lines in the lower panel of Figure 1. The reorientation of the relative direction (or relative phase shift of $\pi$) of the underlying monomer plasmons comprising the hybridized dimer plasmon as it transitions from super-radiant to subradiant character is clearly visible across this limited spectral range. A set of averaged plasmon polarization vectors (white arrows) are overlaid on the EEL maps corresponding to an electron beam placed at the × to aid in visualization. Such a phase flip of the plasmon's polarization is distinguished by the increased EEL probability in the dimer junction[19] at higher energies and is echoed in the CL intensity. This demonstrates that, for this system, the two electron-driven spectroscopies are correlated both spatially and spectrally for certain position of the exciting electron beam.

## CONCLUSION

Through numerical simulation, we have predicted the signatures of Fano interferences in the EELS and CL

of symmetry-broken nanorod dimers that are heterogeneous in material composition and asymmetric in length. The mechanism underlying this electron-driven interference effect is different from that occurring in the optical case: We have discovered that the electron beam of a STEM, depending upon its position, may pin the local orientation of a nanostructure's induced polarization. As a consequence, it is the polarizations of the more distant components that are forced to flip their phase by $\pi$ to accommodate the hybridized (global) plasmon configuration that is resonant at a given value of the EEL. This polarization phase flip generates a corresponding interference in the induced electric near- and far-fields that can show up in EELS, CL, and sometimes in optical spectroscopy as Fano interferences. On the basis of these ideas, we have further predicted a new class of Fano resonances that are uniquely electron-driven and are absent in the optical response.

## METHODS

**Electron Energy Loss and Cathodoluminescence Simulations.** The coupled-dipole[35] or DDA[36] approach is routinely used to study the response of metal nanoparticles subjected to optical frequency radiation.[38] In our previous work, we developed and numerically implemented the *e*-DDA[19,39] as a generalization of this approximation, incorporating the electron beam of a STEM in place of a plane-polarized electric field source as is common to the DDA. In the *e*-DDA, the target is discretized into a finite collection of polarizable point dipoles $\mathbf{P}_j$, $1 \leq j \leq N$, each driven by the evanescent electric field

$$\mathbf{E}_{\text{electron}}(\mathbf{x}, \omega) = \frac{2e\omega}{v^2\varepsilon\gamma} e^{i\omega z/v}\left[\frac{i}{\gamma}K_0\left(\frac{\omega b}{v\gamma}\right)\hat{\mathbf{v}} - K_1\left(\frac{\omega b}{v\gamma}\right)\hat{\mathbf{b}}\right] \quad (4)$$

of a passing swift electron as well as by the fully retarded electric dipole field $\Sigma_{j\neq i}^{N}\mathbf{\Lambda}_{ij}\mathbf{P}_j$ generated by all other points; here $\mathbf{\Lambda}_{ij} = e^{ikr_{ij}}\{(1/r_{ij}^3 - ik/r_{ij}^2)[3\hat{\mathbf{n}}_{ij}\hat{\mathbf{n}}_{ij} - 1_{ij}] - k^2\hat{\mathbf{n}}_{ij}\times(\hat{\mathbf{n}}_{ij}\times)/r_{ij}\}$ is the standard dipole tensor that relays the electric field generated by a dipole at one point in space $\mathbf{x}_i$ to another $\mathbf{x}_j$ a distance $r_{ij}\hat{\mathbf{n}}_{ij} = |\mathbf{x}_i - \mathbf{x}_j|\hat{\mathbf{n}}_{ij}$ away. In this manner, the electron-induced responses of the system can be computed once each dipole is brought into self-consistency with all others at a certain value of the electron's loss energy, $\hbar\omega$. This is accomplished through the iterative solution of the following equation

$$\sum_{j=1}^{N}[\boldsymbol{\alpha}_{ii}^{-1}(\omega)\delta_{ij} - (1-\delta_{ij})\mathbf{\Lambda}_{ij}]\cdot\mathbf{P}_j(\omega) = \mathbf{E}_{\text{electron}}(\mathbf{x}_i, \omega) \quad (5)$$

and depends upon the frequency-dependent linear polarizability $\boldsymbol{\alpha}_{ij}(\omega) \equiv \boldsymbol{\alpha}_{ii}(\varepsilon(\omega))\delta_{ij}$ of the target point *i*. The polarizability is related to the dielectric function through the lattice dispersion relation[40] and includes the effects of radiation reaction.[36] The electric field of the electron[41] in eq 4 depends upon the modified Bessel functions of the second kind $K_0$ and $K_1$, the Lorentz contraction factor $\gamma = 1/(1 - \varepsilon(v/c)^2)^{1/2}$, and the dielectric function $\varepsilon$ of the background medium, which is taken to be vacuum in all calculations. The incident velocity $\mathbf{v} = v\hat{\mathbf{v}}$ of the electron is determined by its incident kinetic energy $m\gamma c^2 - mc^2$ and is oriented along the *z* axis ($\hat{\mathbf{z}} \| \hat{\mathbf{v}}$). We choose the phase $e^{i\omega z/v} = 1$ at the *z*-height of the mass centroid of the target, which defines the plane of the impact parameter $\mathbf{b} = b\hat{\mathbf{b}}$, with $\mathbf{x} = (\mathbf{b}, z)$ that is perpendicular to the electron beam and that contains this point.

Other approaches to simulating EELS rely on different numerical methods of varying efficiency. The *e*-DDA benefits from the requirement that only the target needs to be discretized. The source field of the electron as well as the scattered fields of each target dipole are all known analytically. Finite-element-based methods, such as the COMSOL implementation,[21] require both the target and surrounding medium to be discretized into elements, with all fields and associated boundary conditions represented numerically on the grid. Both approaches should result in the same observable quantities as long as all relevant convergence criteria are met.

All target structures investigated *via* *e*-DDA simulations are excited by a 0.10 MeV electron beam directed normal to the longitudinal axis of the rod; the corresponding velocity of the electrons in the beam is 0.55*c*. Only aloof trajectories through vacuum are considered in the simulations, and the two-dimensional grid of impact parameters **b** for the electron beam is chosen to have a 1 nm spacing. Dielectric data from Johnson and Christy[42] are used for Ag and from the SOPRA database[43] for Pd. An interdipole spacing of 1 nm is used for the target; other dipole spacings were tested to ensure that all spectra are converged at this value.

The most recent version of the *e*-DDA code[39] computes CL spectra and spatial maps in addition to EEL properties. The electron-induced response, $\mathbf{P}_j$, of the target is solved at each spatial position of the electron beam according to eq 5 as in the previous version of our code. However, for CL, at each spatial position of the beam and at each value of the loss energy, the induced electric field $\mathbf{E}_{\text{ind}}$ is computed according to

$$\mathbf{E}_{\text{ind}}(\mathbf{x}, \omega) = \sum_{j=1}^{N}\mathbf{\Lambda}(\mathbf{x}, \mathbf{x}_j)\cdot\mathbf{P}_j(\omega) \quad (6)$$

at various points **x** in the far-field. For the *e*-DDA-based CL calculations performed in this article, $\mathbf{E}_{\text{ind}}$ is computed on an angular grid of points spanning the surface of distant sphere of radius 5 $\mu$m, with 75 points in $\theta$ and 75 points in $\phi$. In this way, either the differential CL response $d\Gamma_{CL}/d\Omega$ or, by quadratured solid-angle integration, the total CL response $\Gamma_{CL}$ may be computed.

*Conflict of Interest:* The authors declare no competing financial interest.

*Acknowledgment.* This work was supported by the University of Washington, the University of Tennessee, the UT/ORNL Joint Institute for Advanced Materials, the U.S. Department of Energy, Office of Basic Energy Sciences under Award Number DE-SC0004792 (J.P.C.), and the National Science Foundation's CAREER program under Award Number CHE-1253775 (D.J.M.).

## REFERENCES AND NOTES

1. Fano, U. Effects of Configuration Interaction on Intensities and Phase Shifts. *Phys. Rev.* **1961**, *124*, 1866–1878.
2. Lassiter, J. B.; Sobhani, H.; Knight, M. W.; Mielczarek, W. S.; Nordlander, P.; Halas, N. J. Designing and Deconstructing the Fano Lineshape in Plasmonic Nanoclusters. *Nano Lett.* **2012**, *12*, 1058–1062.
3. Verellen, N.; Sonnefraud, Y.; Sobhani, H.; Hao, F.; Moshchalkov, V. V.; Van Dorpe, P.; Nordlander, P.; Maier, S. A. Fano Resonances in Individual Coherent Plasmonic Nanocavities. *Nano Lett.* **2009**, *9*, 1663–1667.
4. Guillaume, S. O.; Geuquet, N.; Henrard, L. Numerical Study of Optical and EELS Response of Coupled Metallic Nanoparticles. *Proc. SPIE* **2011**, *8089*, 7.
5. Sonnefraud, Y.; Verellen, N.; Sobhani, H.; Vandenbosch, G. A. E.; Moshchalkov, V. V.; Van Dorpe, P.; Nordlander, P.; Maier, S. A. Experimental Realization of Subradiant, Superradiant, and Fano Resonances in Ring/Disk Plasmonic Nanocavities. *ACS Nano* **2010**, *4*, 1664–1670.
6. Sheikholslami, S. N.; García-Etxarri, A.; Dionne, J. A. Controlling the Interplay of Electric and Magnetic Modes *via* Fano-like Plasmon Resonances. *Nano Lett.* **2011**, *11*, 3927–3934.

7. Suenaga, K.; Sato, Y.; Liu, Z.; Kataura, H.; Okazaki, T.; Kimoto, K.; Sawada, H.; Sasaki, T.; Omoto, K.; Tomita, T.; *et al.* Visualizing and Identifying Single Atoms using Electron Energy-Loss Spectroscopy with Low Accelerating Voltage. *Nat. Chem.* **2009**, *1*, 415–418.
8. García de Abajo, F. J. Optical Excitations in Electron Microscopy. *Rev. Mod. Phys.* **2010**, *82*, 209.
9. Nellist, P. D.; Pennycook, S. J. Subangstrom Resolution by Underfocused Incoherent Transmission Electron Microscopy. *Phys. Rev. Lett.* **1998**, *81*, 4156.
10. Mazzucco, S.; Geuquet, N.; Ye, J.; Stéphan, O.; Van Roy, W.; Van Dorpe, P.; Henrard, L.; Kociak, M. Ultralocal Modification of Surface Plasmons Properties in Silver Nanocubes. *Nano Lett.* **2012**, *12*, 1288–1294.
11. Scholl, J. A.; Koh, A.; Dionne, J. A. Quantum Plasmon Resonances of Individual Metallic Nanoparticles. *Nature* **2012**, *483*, 421.
12. Koh, A. L.; Bao, K.; Khan, I.; Smith, W. E.; Kothleitner, G.; Nordlander, P.; Maier, S. A.; McComb, D. W. Electron Energy-Loss Spectroscopy (EELS) of Surface Plasmons in Single Silver Nanoparticles and Dimers: Influence of Beam Damage and Mapping of Dark Modes. *ACS Nano* **2009**, *3*, 3015–3022.
13. Schaffer, B.; Grogger, W.; Kothleitner, G.; Hofer, F. Comparison of EFTEM and STEM EELS Plasmon Imaging of Gold Nanoparticles in a Monochromated TEM. *Ultramicroscopy* **2010**, *110*, 1087–1093.
14. Nelayah, J.; Kociak, M.; Stéphan, O.; García de Abajo, F. J.; Tencé, M.; Hendrard, L.; Taverna, D.; Pastoriza-Santos, I.; Liz-Marzán, L. M.; Colliex, C. Mapping Surface Plasmons on a Single Metallic Nanoparticle. *Nat. Phys.* **2007**, *3*, 348–353.
15. Bourdarham, G.; Feth, N.; Myroshnychenko, V.; Linden, S.; García de Abajo, J.; Wegener, M.; Kociak, M. Spectral Imaging of Individual Split-Ring Resonators. *Phys. Rev. Lett.* **2010**, *105*, 255501.
16. Bosman, M.; Ye, E.; Tan, S. F.; Nijhuis, C. A.; Yang, J. K. W.; Marty, R.; Mlayah, A.; Arbouet, A.; Girard, C.; Han, M. Y. Surface Plasmon Damping Quantified with an Electron Nanoprobe. *Sci. Rep.* **2012**, *3*, 1312.
17. Nicoletti, O.; Wubs, M.; Mortensen, N. A.; Sigle, W.; van Aken, P. A.; Midgley, P. A. Surface Plasmon Modes of a Single Silver Nanorod: An Electron Energy Loss Study. *Opt. Express* **2011**, *19*, 15371–15379.
18. Guiton, B. S.; Iberi, V.; Li, S.; Leonard, D. N.; Parish, C. M.; Kotula, P. G.; Varela, M.; Schatz, G. C.; Pennycook, S. J.; Camden, J. P. Correlated Optical Measurements and Plasmon Mapping of Silver Nanorods. *Nano Lett.* **2011**, *11*, 3482–3488.
19. Bigelow, N. W.; Vaschillo, A.; Iberi, V.; Camden, J. P.; Masiello, D. J. Characterization of the Electron- and Photon-Driven Plasmonic Excitations of Metal Nanorods. *ACS Nano* **2012**, *6*, 7497–7504.
20. Mirsaleh-Kohan, N.; Iberi, V.; Simmons, P. D.; Bigelow, N. W.; Vaschillo, A.; Rowland, M. M.; Best, M. D.; Pennycook, S. J.; Masiello, D. J.; Guiton, B. S.; *et al.* Single-Molecule Surface-Enhanced Raman Scattering: Can STEM/EELS Image Electromagnetic Hot Spots? *J. Phys. Chem. Lett.* **2012**, *3*, 2303–2309.
21. Koh, A. L.; Fernández-Domínguez, A. I.; McComb, D. W.; Maier, S. A.; Yang, J. K. W. High-Resolution Mapping of Electron-Beam-Excited Plasmon Modes in Lithographically Defined Gold Nanostructures. *Nano Lett.* **2011**, *11*, 1323–1330.
22. Alber, I.; Sigle, W.; Müller, S.; Neumann, R.; Picht, O.; Rauber, M.; van Aken, P. A.; Toimil-Molares, M. E. Visualization of Multipolar Longitudinal and Transversal Surface Plasmon Modes in Nanowire Dimers. *ACS Nano* **2011**, *5*, 9845–9853.
23. Alber, I.; Sigle, W.; Demming-Janssen, F.; Neumann, R.; Trautmann, C.; van Aken, P. A.; Toimil-Molares, M. E. Multipole Surface Plasmon Resonances in Conductively Coupled Metal Nanowire Dimers. *ACS Nano* **2012**, *6*, 9711–9717.
24. Yamamoto, Y.; Araya, K.; García de Abajo, F. J. Photon Emission from Silver Particles Induced by a High-Energy Electron Beam. *Phys. Rev. B* **2001**, *64*, 9.
25. Vesseur, E. J. R.; de Waele, R.; Kuttge, M.; Polman, A. Direct Observation of Plasmonic Modes in Au Nanowires Using High-Resolution Cathodoluminescence Spectroscopy. *Nano Lett.* **2007**, *7*, 2843–2846.
26. Gómez-Medina, R.; Yamamoto, N.; Nakano, M.; García de Abajo, F. J. Mapping Plasmons in Nanoantennas *via* Cathodoluminescence. *New J. Phys.* **2008**, *10*, 105009.
27. García de Abajo, F. J.; Kociak, M. Probing the Photonic Local Density of States with Electron Energy Loss Spectroscopy. *Phys. Rev. Lett.* **2008**, *100*, 106804.
28. Hohenester, U.; Ditlbacher, H.; Krenn, J. R. Electron-Energy-Loss Spectra of Plasmonic Nanoparticles. *Phys. Rev. Lett.* **2009**, *103*, 106801.
29. Lazar, S.; Botton, G. A.; Zandbergen, H. W. Enhancement of Resolution in Core-Loss and Low-Loss Spectroscopy in a Monochromated Microscope. *Ultramicroscopy* **2006**, *11*, 1091–1103.
30. Schaffer, B.; Hohenester, U.; Trügler, A.; Hofer, F. High-Resolution Surface Plasmon Imaging of Gold Nanoparticles by Energy-Filtered Transmission Electron Microscopy. *Phys. Rev. B* **2009**, *79*, 041401.
31. Krivanek, O. L.; Ursin, J. P.; Bacon, N. J.; Corbin, G. J.; Dellby, N.; Hrncirik, P.; Murfitt, M. F.; Own, C. S.; Szilagyi, Z. S. High-Energy-Resolution Monochromator for Aberration-Corrected Scanning Transmission Electron Microscopy/Electron Energy-Loss Spectroscopy. *Philos. Trans. R. Soc., A* **2009**, *367*, 3683–3697.
32. Hao, F.; Sonnefraud, Y.; Dorpe, P. V.; Maier, S. A.; Halas, N. J.; Nordlander, P. Symmetry Breaking in Plasmonic Nanocavities: Subradiant LSPR Sensing and a Tunable Fano Resonance. *Nano Lett.* **2008**, *8*, 3983–3988.
33. Liu, N.; Weiss, T.; Mesch, M.; Langguth, L.; Eigenthaler, U.; Hirscher, M.; Sönnichsen, C.; Giessen, H. Planar Metamaterial Analogue of Electromagnetically Induced Transparency for Plasmonic Sensing. *Nano Lett.* **2010**, *10*, 1103–1107.
34. Lassiter, J. B.; Sobhani, H.; Fan, J. A.; Kundu, J.; Capasso, F.; Nordlander, P.; Halas, N. J. Fano Resonances in Plasmonic Nanoclusters: Geometrical and Chemical Tunability. *Nano Lett.* **2010**, *10*, 3184–3189.
35. Purcell, E. M.; Pennypacker, C. R. Scattering and Absorption of Light by Nonspherical Dielectric Grains. *Astrophys. J.* **1973**, *186*, 705.
36. Draine, B. T.; Flatau, P. J. Discrete-Dipole Approximation for Scattering Calculations. *J. Opt. Soc. Am. A* **1994**, *11*, 1491.
37. Alzar, C. L. G.; Martinez, M. A. G.; Nussenzveig, P. Classical Analog of Electromagnetically Induced Transparency. *Am. J. Phys.* **2002**, *70*, 37–41.
38. Kelly, K. L.; Coronado, E.; Zhao, L. L.; Schatz, G. C. The Optical Properties of Metal Nanoparticles: The Influence of Size, Shape, and Dielectric Environment. *J. Phys. Chem. B* **2003**, *107*, 668.
39. Masiello Group Website, Theory of Molecular Plasmonics and Optics on the Nanoscale; http://faculty.washington.edu/masiello.
40. Draine, B. T.; Goodman, J. Beyond Clausius-Mossotti: Wave Propagation on a Polarizable Point Lattice and the Discrete Dipole Approximation. *Astrophys. J.* **1993**, *405*, 685.
41. Jackson, J. D. *Classical Electrodynamics*, 3rd ed.; John Wiley & Sons: New York, 1999.
42. Johnson, P. B.; Christy, R. W. Optical Constants of the Noble Metals. *Phys. Rev. B* **1972**, *6*, 4370.
43. SOPRA n&k Optical Database (available at http://www.sopra-sa.com/more/database.asp).